

# Multiwavelength three-dimensional near-infrared tomography of the breast: initial simulation, phantom, and clinical results

Hamid Dehghani, Brian W. Pogue, Steven P. Poplack, and Keith D. Paulsen

Three-dimensional (3D), multiwavelength near-infrared tomography has the potential to provide new physiological information about biological tissue function and pathological transformation. Fast and reliable measurements of multiwavelength data from multiple planes over a region of interest, together with adequate model-based nonlinear image reconstruction, form the major components of successful estimation of internal optical properties of the region. These images can then be used to examine the concentration of chromophores such as hemoglobin, deoxyhemoglobin, water, and lipids that in turn can serve to identify and characterize abnormalities located deep within the domain. We introduce and discuss a 3D modeling method and image reconstruction algorithm that is currently in place. Reconstructed images of optical properties are presented from simulated data, measured phantoms, and clinical data acquired from a breast cancer patient. It is shown that, with a relatively fast 3D inversion algorithm, useful images of optical absorption and scatter can be calculated with good separation and localization in all cases. It is also shown that, by use of the calculated optical absorption over a range of wavelengths, the oxygen saturation distribution of a tissue under investigation can be deduced from oxygenated and deoxygenated hemoglobin maps. With this method the reconstructed tumor from the breast cancer patient was found to have a higher oxy-deoxy hemoglobin concentration and also a higher oxygen saturation level than the background, indicating a ductal carcinoma that corresponds well to histology findings. © 2003 Optical Society of America

*OCIS codes:* 170.3010, 110.6880, 170.3830, 170.6960.

## 1. Introduction

Near-infrared (NIR) optical tomography is a noninvasive imaging technique that can be used to interrogate the optical properties of biological tissue, particularly the peripheral muscles, the neonatal brain, and the breast.<sup>1–10</sup> An optical fiber placed on the surface of the region of interest delivers an input optical signal (continuous,<sup>11</sup> amplitude modulated,<sup>12</sup> or ultrashort pulses<sup>5</sup>) while other optical fibers placed at different locations on the same surface detect the outcoming photons that have propagated through the volume under investigation. The intensity and

path-length distributions of the exiting photons provide information about the optical properties of the transilluminated tissue by use of a model-based interpretation in which photon propagation is simulated by diffusion theory. Through an iterative solution to match the theoretical prediction to the actual measured values, the images of internal absorption and scattering coefficient distribution can be reconstructed.

Our main interest lies in the detection and characterization of tumors within the female breast.<sup>2</sup> Inasmuch as the absorption and scattering of light in tissue are functions of the tissue's optical properties and hence of its physiological state, our aim is to obtain images of internal optical absorption ( $\mu_a$ ), reduced scattering ( $\mu_s'$ ), and ultimately images of total hemoglobin and oxygen saturation ( $\text{HbO}_2$ ,  $\text{Hb}$ , and  $\text{SO}_2$ ) distributions. These images should in principle provide information about the physiological state of the tissue under investigation and help to identify and characterize tumors within the breast.

Despite evidence of high contrast, NIR imaging is confounded by a dominant scattering that serves to

H. Dehghani (hamid.dehghani@dartmouth.edu), B. W. Pogue, and K. Paulsen are with the Thayer School of Engineering, Dartmouth College, Hanover, New Hampshire 03755. S. P. Poplack is with the Department of Radiology, Dartmouth-Hitchcock Medical Center, Lebanon, New Hampshire 03766.

Received 14 May 2002; revised manuscript received 12 September 2002.

0003-6935/03/010135-11\$15.00/0

© 2003 Optical Society of America

limit its spatial resolution. Light is attenuated similarly for both absorption and scattering heterogeneities, making quantitative absorption imaging a challenging task. The use of frequency-domain and time-resolved techniques to obtain path-length information, in combination with model-based iterative reconstruction methods, allows for the separation of absorption and scattering heterogeneities<sup>13</sup> and improves spatial resolution and contrast.<sup>14</sup> Currently the resolution limits of the NIR method are unclear; however, moderate-resolution quantitative images of absorption, scattering, and hemoglobin parameters<sup>15</sup> have been obtained in phantom studies, which suggests that clinically useful quantitative hemoglobin imaging can be achieved *in vivo*.<sup>16</sup>

Several groups of researchers worldwide are pursuing NIR imaging of the breast for tumor characterization.<sup>4,11,16–20</sup> Some studies have anecdotally obtained similar sensitivity and specificity to x-ray mammography, but, considering the widespread placement, acceptance, and the low dose rates of modern x-ray machines, other NIR studies have been discontinued.<sup>20</sup> However, a critical concern in these discontinued studies was the lack of a rigorous image reconstruction algorithm that would optimize the sensitivity and specificity of the system before completion of these types of clinical efficacy trial. Recently a clinical demonstration of the detection of changes in  $\mu_a$  from continuous-wave data<sup>11</sup> by means of a three-dimensional (3D) reconstruction algorithm was been reported. However, in that research the authors did not recover  $\mu_s'$  properties or the spatial distribution of HbO<sub>2</sub>, Hb, or SO<sub>2</sub>. Interest remains in 3D NIR quantitative hemoglobin imaging, dynamic imaging, imaging with contrast agents, and incorporation of structural information from high-resolution imaging modalities to improve the resolution and accuracy of NIR hemoglobin images. Not surprisingly, it is the measurement of hemoglobin content and oxygen saturation (a surrogate for tumor neovascularity) that provides the best opportunity for supplying new information that is unavailable from use of conventional techniques, i.e., mammography and breast sonography.

We describe a 3D modeling technique and reconstruction algorithm for amplitude modulated frequency-domain NIR imaging that simultaneously recovers volumetric maps of  $\mu_a$  and  $\mu_s'$ . 3D reconstruction of simulated data is presented, followed by phantom data. The study concludes with 3D multiwavelength reconstructed images of  $\mu_a$  and  $\mu_s'$  together with 3D maps of HbO<sub>2</sub>, Hb, and oxygen saturation from data collected from a female volunteer with cancer of the breast.

## 2. Method

Under the assumption that scattering dominates absorption in a region of interest, the Boltzmann transport equation can be simplified to a diffusion

approximation that in the frequency domain is given by

$$-\nabla \cdot \kappa(\mathbf{r}) \nabla \Phi(\mathbf{r}, \omega) + \left[ \mu_a(\mathbf{r}) + \frac{i\omega}{c} \right] \Phi(\mathbf{r}, \omega) = q_0(\mathbf{r}, \omega), \quad (1)$$

where  $q_0(\mathbf{r}, \omega)$  is an isotropic source,  $\Phi(\mathbf{r}, \omega)$  is the photon density at position  $\mathbf{r}$ , and  $\kappa = 1/3(\mu_a + \mu_s')$  is the diffusion coefficient. We use the Robin-type (type III) boundary condition:

$$\Phi(\gamma) + \frac{\kappa}{\alpha} \hat{\mathbf{n}} \cdot \nabla \Phi(\gamma) = 0, \quad (2)$$

where  $\alpha$  is a term that incorporates reflection as a result of refractive-index mismatch<sup>21</sup> at the boundary and  $\hat{\mathbf{n}}$  is the outer normal to the boundary ( $\partial\Omega$ ) at  $\gamma$ .

We assume that the data are represented by a nonlinear operator  $\mathbf{y}^* = \mathbf{F}(\mu_a, \kappa)$ , where our datum  $\mathbf{y}^*$  is a complex vector that has real and imaginary components, which are mapped to log amplitude and phase in measurement. Then the image reconstruction method seeks a solution

$$(\hat{\mu}_a, \hat{\kappa}) = \arg \min_{\mu_a, \kappa} \|\mathbf{y}^* - \mathbf{F}(\mu_a, \kappa)\|_W^2, \quad (3)$$

where  $\|\cdot\|_W^2$  is the  $L_2$  norm with weight  $W$ . This magnitude is sometimes referred to as the projection error and provides a value with which to determine the validity of the iterative reconstruction algorithm.

We use a finite-element method as a general and flexible method for solving the forward problem in arbitrary geometries.<sup>22,23</sup> In the inverse problem, in which we aim to recover internal optical property distributions from boundary measurements, we assume that  $\mu_a(\mathbf{r})$  and  $\kappa(\mathbf{r})$  are expressed in a basis with a limited number of dimensions (fewer than the number of dimensions of the finite-element system matrices). A number of strategies for defining reconstruction basis are possible; in this paper we use a second mesh basis,<sup>24</sup> whose local shape and continuity characteristics are the same as those of the original mesh but with fewer degrees of freedom. To find  $(\hat{\mu}_a, \hat{\kappa})$  in Eq. (3) we used a Levenberg–Marquardt algorithm, in which we repeatedly solve

$$\mathbf{a} = J^T(JJ^T + \rho I)^{-1}\mathbf{b}, \quad (4)$$

where  $\mathbf{b}$  is the data vector,  $\mathbf{b} = [\mathbf{y}^* - \mathbf{F}(\mu_a, \kappa)]^T$ ,  $\mathbf{a}$  is the solution update vector,  $\mathbf{a} = [\delta\kappa(j); \delta\mu_a(j)]$ , and  $j$  is the number of the reconstructed basis.  $\rho$  is the regularization factor and  $J$  is the Jacobian matrix for our model, which is calculated by the Adjoint method.<sup>25</sup> Equation (4) is known as the (regularized) underdetermined version of the Moore–Penrose generalized inverse and is found to be highly suitable for 3D problems for which the number of unknowns to be recovered is much larger than the amount of information (measurements) available.<sup>26</sup>

The Jacobian has the form

$$J = \begin{bmatrix} \frac{\delta \ln I_1}{\delta \kappa_1} & \frac{\delta \ln I_1}{\delta \kappa_2} & \dots & \frac{\delta \ln I_1}{\delta \kappa_j} & \frac{\delta \ln I_1}{\delta \mu_{a1}} & \frac{\delta \ln I_1}{\delta \mu_{a2}} & \dots & \frac{\delta \ln I_1}{\delta \mu_{aj}} \\ \frac{\delta \theta_1}{\delta \kappa_1} & \frac{\delta \theta_1}{\delta \kappa_2} & \dots & \frac{\delta \theta_1}{\delta \kappa_j} & \frac{\delta \theta_1}{\delta \mu_{a1}} & \frac{\delta \theta_1}{\delta \mu_{a2}} & \dots & \frac{\delta \theta_1}{\delta \mu_{aj}} \\ \frac{\delta \ln I_2}{\delta \kappa_1} & \frac{\delta \ln I_2}{\delta \kappa_2} & \dots & \frac{\delta \ln I_2}{\delta \kappa_j} & \frac{\delta \ln I_2}{\delta \mu_{a1}} & \frac{\delta \ln I_2}{\delta \mu_{a2}} & \dots & \frac{\delta \ln I_2}{\delta \mu_{aj}} \\ \frac{\delta \ln I_2}{\delta \kappa_1} & \frac{\delta \ln I_2}{\delta \kappa_2} & \dots & \frac{\delta \ln I_2}{\delta \kappa_j} & \frac{\delta \ln I_2}{\delta \mu_{a1}} & \frac{\delta \ln I_2}{\delta \mu_{a2}} & \dots & \frac{\delta \ln I_2}{\delta \mu_{aj}} \\ \vdots & \vdots & \vdots & \vdots & \vdots & \vdots & \vdots & \vdots \\ \frac{\delta \ln I_S}{\delta \kappa_1} & \frac{\delta \ln I_S}{\delta \kappa_2} & \dots & \frac{\delta \ln I_S}{\delta \kappa_j} & \frac{\delta \ln I_S}{\delta \mu_{a1}} & \frac{\delta \ln I_S}{\delta \mu_{a2}} & \dots & \frac{\delta \ln I_S}{\delta \mu_{aj}} \\ \frac{\delta \theta_S}{\delta \kappa_1} & \frac{\delta \theta_S}{\delta \kappa_2} & \dots & \frac{\delta \theta_S}{\delta \kappa_j} & \frac{\delta \theta_S}{\delta \mu_{a1}} & \frac{\delta \theta_S}{\delta \mu_{a2}} & \dots & \frac{\delta \theta_S}{\delta \mu_{aj}} \\ \frac{\delta \kappa_1}{\delta \mu_{a1}} & \frac{\delta \kappa_1}{\delta \mu_{a2}} & \dots & \frac{\delta \kappa_1}{\delta \mu_{aj}} & \frac{\delta \mu_{a1}}{\delta \mu_{a1}} & \frac{\delta \mu_{a1}}{\delta \mu_{a2}} & \dots & \frac{\delta \mu_{a1}}{\delta \mu_{aj}} \end{bmatrix}, \quad (5)$$

where  $\delta \ln I_i / \delta \kappa_j$  and  $\delta \ln I_i / \delta \mu_{aj}$  are the submatrices that define the relation between the log of the amplitude of the  $i$ th measurement with respect to  $\kappa$  and  $\mu_a$  at the  $j$ th reconstructed node, respectively,  $\delta \theta_i / \delta \kappa_j$  and  $\delta \theta_i / \delta \mu_{aj}$  are the submatrices that define the relation between the phase of the  $i$ th measurement with respect to  $\kappa$  and  $\mu_a$  at the  $j$ th reconstructed node, respectively, and  $S$  is the total number of measurements.

### 3. Results

In the following subsections, three categories of reconstruction results are presented that differ in terms of the boundary data that they employ. Specifically, we demonstrate successful image reconstruction from

3D data generated from a finite-element model of a cylindrical phantom containing a single  $\mu_a$  anomaly and a single  $\mu_s'$  anomaly. These data are used to indicate the capabilities of the reconstruction algorithm under ideal conditions.

3D data acquired with our frequency-domain instrument<sup>12,27</sup> from a cylindrical phantom containing a single  $\mu_a$  and  $\mu_s'$  anomaly. These data are used to demonstrate the capabilities of the reconstruction algorithm when measured data obtained during a controlled situation are used.

3D multiwavelength data measured with the frequency-domain instrument during a clinical breast exam of a patient diagnosed with a malignant tumor. These data are used to highlight the capabilities of the reconstruction algorithm when measured data from a patient in a clinical setup are used.

#### A. Reconstruction from Simulated Data

The synthetic boundary data at a modulation frequency of 100 MHz were calculated for a cylindrical phantom containing a single  $\mu_a$  anomaly and a single  $\mu_s'$  anomaly. The cylinder had a radius of 43 mm and a height of 40 mm, centered at  $x, y, z = 0$  mm. The mesh was generated with the NETGEN generator<sup>28</sup> and contained a total of 8990 nodes, which cor-

responded to 44,803 linear tetrahedral elements [see Fig. 1(a)]. The model had a background of  $\mu_a = 0.01 \text{ mm}^{-1}$  and  $\mu_s' = 1.0 \text{ mm}^{-1}$ . The  $\mu_a$  anomaly was positioned at  $x = -20 \text{ mm}$ ,  $y = 0 \text{ mm}$ ,  $z = -10 \text{ mm}$  and had a radius of 5 mm and  $\mu_a = 0.03 \text{ mm}^{-1}$ ; the  $\mu_s'$  anomaly was located at  $x = 20 \text{ mm}$ ,  $y = 0 \text{ mm}$ ,  $z = 10 \text{ mm}$  and had a radius of 5 mm and  $\mu_s' = 3.0 \text{ mm}^{-1}$ . A total of 48 sources and 48 measurement sites spanned 3 planes,  $z = 10, 0, -10 \text{ mm}$ , with 16 source and detector fibers in each plane. The sources were modeled as isotropic Gaussian distributions with a full width at half-maximum of 3 mm placed one scattering distance (1 mm) inside the outer boundary. As our instrumentation is not currently configured to measure out-of-plane data, we utilized only in-plane data that were due to each source, which yielded a total of 720 measurements (15 detectors  $\times$  16 sources  $\times$  3 planes).

3D images of internal properties were calculated from these measurements with Eq. (4). The initial homogeneous values used for the reconstruction were those of the background at  $\mu_a = 0.01 \text{ mm}^{-1}$  and  $\mu_s' = 1.0 \text{ mm}^{-1}$ . The reconstruction basis employed a second mesh of the same physical dimensions as the forward mesh but that contained 3112 nodes and 14,873 linear tetrahedral elements [Fig. 1(b)]. The regularization parameter,  $\rho$ , was initially set to 10 and was varied at each iteration by a factor of  $10^{1/4}$  if the projection error [Eq. (3)] was less than in the previous iteration. If the projection error was found to increase,  $\rho$  increased by a factor of  $10^{1/8}$ . This approach was found to be relatively stable; it allows the reconstruction algorithm to choose the regularization level, depending on the value of the projection error.

The reconstructed images at the 9th iteration are shown in Fig. 2. In Fig. 2, both  $\mu_a$  and  $\mu_s'$  images have been reconstructed with minimum background artifact and good property separation. Calculated background  $\mu_a$  is  $0.0089 \text{ mm}^{-1}$ , and  $\mu_s'$  is  $0.96 \text{ mm}^{-1}$ , which corresponds well to values of the target image. The peak value for the  $\mu_a$  image is  $0.0124 \text{ mm}^{-1}$  (at

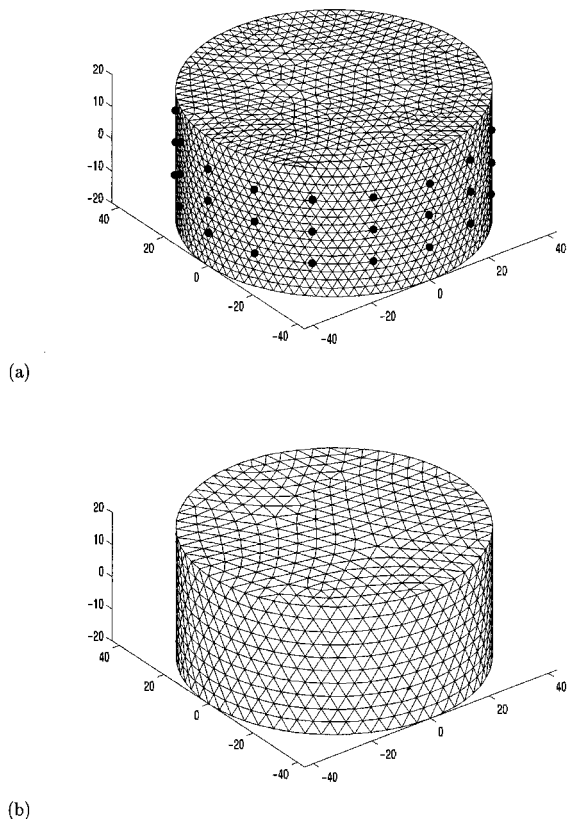


Fig. 1. Meshes used for reconstruction of images from simulated data. (a) Cylindrical mesh used for the calculation of the simulated data. The cylinder had a radius of 43 mm and a height of 40 mm and contained a total of 8990 nodes, corresponding to 44,803 linear tetrahedral elements. (b) Cylindrical mesh used for the reconstruction. The cylinder had radius of 43 mm and a height of 40 mm and contained a total of 3112 nodes, corresponding to 14,873 linear tetrahedral elements.

$z = -10$  mm), and the  $\mu_s'$  image is  $1.3 \text{ mm}^{-1}$  (at  $z = 10$  mm).

#### B. Reconstruction from Measured Phantom Data

The results presented in this subsection are based on data measured from a phantom that uses our frequency-domain system. A hollow phantom of 43-mm radius and 100-mm height was filled with a mixture of Intralipid solution and India ink to produce a uniform background,  $\mu_a = 0.0044 \text{ mm}^{-1}$  and  $\mu_s' = 1.0 \text{ mm}^{-1}$ . Within this phantom a small shiny black marble of 5.5-mm radius was suspended at  $x = 21$  mm,  $y = 0$  mm,  $z = 0$  mm [see Fig. 3]. As in the simulated case, a total of 48 sources and 48 detectors were located in 3 planes,  $z = 10, 0, -10$  mm, with 16 source and measurement sites per plane.

Data were collected at 100 MHz by use of a 785-nm light source. In addition, to facilitate calibration we measured a set of data without the anomaly present. Precise data calibration is an essential part of image reconstruction. Here we describe the basic steps used for calibration:

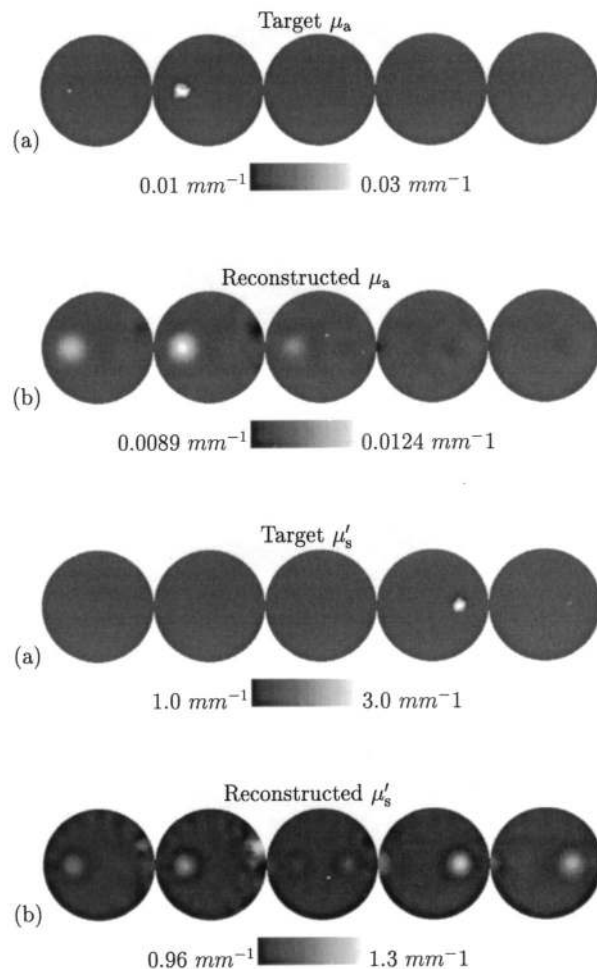


Fig. 2. Target and reconstructed images of  $\mu_a$  and  $\mu_s'$  from simulated data. Each slice represents a plane through the cylindrical mesh from the bottom of the cylinder (leftmost image) to the top (rightmost image). Reconstructed images are shown at the 9th iteration.

1. Using the measured homogeneous data without an anomaly present, we averaged measurements from all sources within each plane to produce 15 measurements per plane,  $data(mean)$ . Here, both phase and amplitude of the data are used. As we have a symmetric circular measurement array,  $data(mean)$  is calculated as

$$data(mean)_d = \frac{1}{NS} \sum_{n=1}^{NS} data_{n,d}, \quad (6)$$

where  $d$  is the number of measurements per source per plane (15 measurements per plane),  $NS$  is the total number of sources per plane, and  $data$  is either log amplitude or phase. From this information, global  $\mu_a$  and  $\mu_s'$  values were estimated that give the best fit to this data with a two step algorithm:

(a) Global  $\mu_a$  and  $\mu_s'$  values were calculated, based on the source-detector separation, by use of an



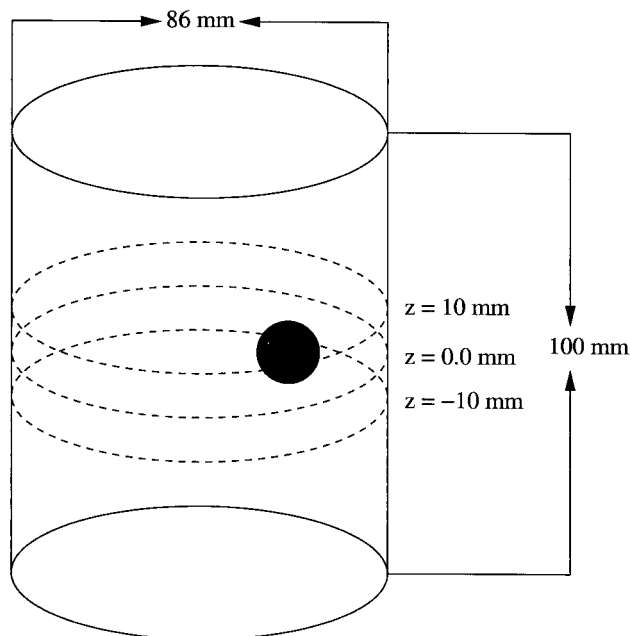


Fig. 3. Outline of the cylindrical phantom used for the collection of data in the presence of a single black shiny marble suspended at  $x = 21$  mm,  $y = 0$  mm,  $z = 0$  mm.

analytical model for an infinite medium coupled to a Newton–Raphson iterative scheme.<sup>27</sup>

(b) Using the values calculated in step (a) as an initial guess, we calculated new global  $\mu_a$  and  $\mu_s'$  values:  $\mu_{a(\text{homog})}$  and  $\mu_{s(\text{homog})}'$ , with a finite-element model of the imaging domain.<sup>27</sup>

2. From the measured data with an anomaly present we repeated the previous steps described for the homogenous case to calculate global  $\mu_a$  and  $\mu_s'$  values for the anomaly data:  $\mu_{a(\text{anom})}$  and  $\mu_{s(\text{anom})}'$ .

3. Using the computed global values, we calculated an offset between the measured homogenous data and the modeled homogenous data [with  $\mu_{a(\text{homog})}$  and  $\mu_{s(\text{homog})}'$ ], namely,  $data_{\text{offset}(\text{homog})}$ , as well as an offset between the measured anomaly data and the modeled anomaly data [with  $\mu_{a(\text{anom})}$  and  $\mu_{s(\text{anom})}'$ ], namely,  $data_{\text{offset}(\text{anom})}$ .

4. Based on the offset values and the homogenous fit, the data were then calibrated from

$$data_{\text{calibrated}(\text{anom})} = data_{\text{measured}(\text{anom})} - [data_{\text{measured}(\text{homog})} - data_{\text{calculated}(\text{homog})}] - [data_{\text{offset}(\text{anom})} - data_{\text{offset}(\text{homog})}]. \quad (7)$$

This stage of the reconstruction algorithm eliminates systematic errors within the data and provides an initial estimate of the optical properties for image recovery that is crucial for convergence of the iterative method [Eq. (4)]. The last term in Eq. (7),  $data_{\text{offset}(\text{anom})} - data_{\text{offset}(\text{homog})}$ , corrects for error that is due system drift if such exists. However, in all our studies this term was found to be very small.

The calculated global values for these sets of mea-

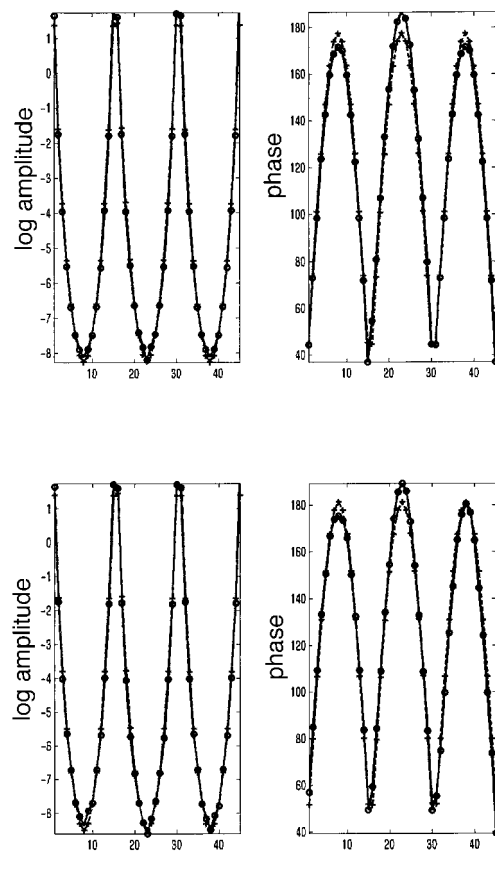


Fig. 4. Plots of the averaged modeled data from each plane of measurements for (a) the homogeneous phantom and (b) the heterogeneous phantom, as shown in Fig. 3. Log amplitude and phase data are shown. Circles, measured results; crosses, modeled values based on the global  $\mu_a$  and  $\mu_s'$  estimates.

sured data were  $\mu_{a(\text{homog})} = 0.0045 \text{ mm}^{-1}$  and  $\mu_{s(\text{homog})}' = 1.1322 \text{ mm}^{-1}$ ,  $\mu_{a(\text{anom})} = 0.0042 \text{ mm}^{-1}$  and  $\mu_{s(\text{anom})}' = 1.1337 \text{ mm}^{-1}$ . Figure 4 shows plots of the average data [calculated from Eq. (6)], per plane, for the measured and modeled results in both the homogeneous and the anomalous cases. In Fig. 4(a) the average data from the homogenous phantom are shown (circles) together with the modeled average data; the finite-element cylindrical phantom and the calculated global average  $\mu_{a(\text{homog})}$  and  $\mu_{s(\text{homog})}'$  values were used. Based on these calibration and fitting procedures, the measured data can be matched to the modeled data, with the log of the amplitude reaching a better fit than the phase. Note that the phase data are not completely symmetric, indicating that these data generally cannot be fitted perfectly by a homogenous model, and the calibration process with  $data_{\text{calibrated}(\text{anom})}$  can minimize this error. In Figure 4(b) the average data from the phantom with the anomaly are shown together with the modeled average data; the cylindrical finite-element phantom and the calculated global average  $\mu_{a(\text{anom})}$  and  $\mu_{s(\text{anom})}'$  values were used. The anomalous data again matched the modeled results well.

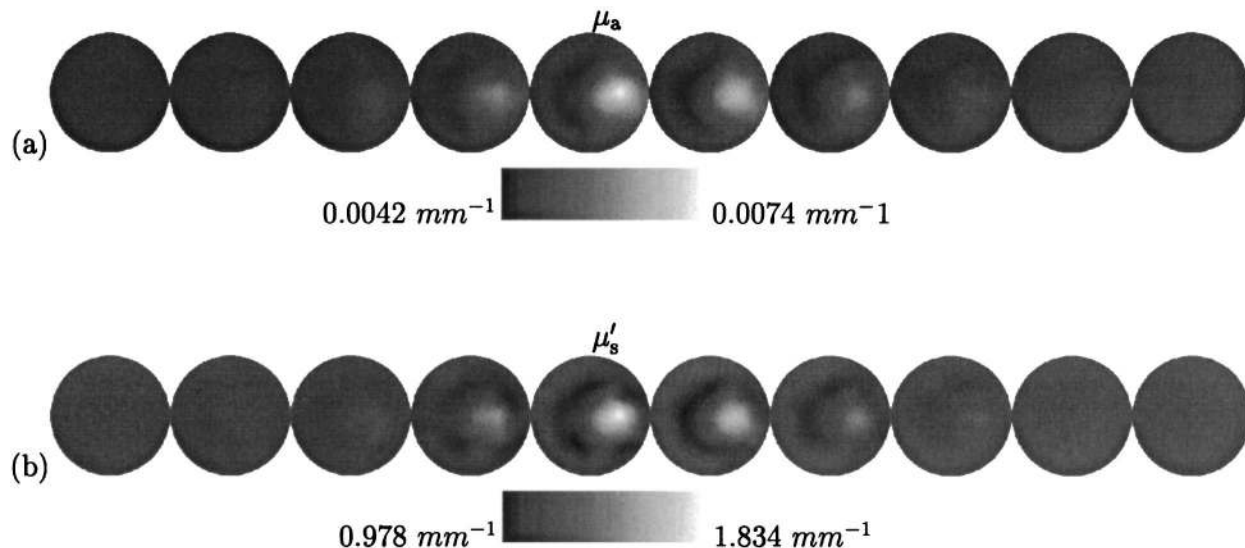


Fig. 5. Reconstructed images at the tenth iteration of  $\mu_a$  and  $\mu_s'$  from measured phantom data. Each slice represents a plane through the cylindrical mesh from the bottom of the cylinder (leftmost image) to the top (rightmost image).

We used the calibrated data,  $data_{calibrated(anom)}$ , together with a finite-element model of the imaging domain to reconstruct images of internal  $\mu_a$  and  $\mu_s'$ . The finite-element mesh that we used to calculate the Jacobian was a cylindrical mesh of 43-mm radius and 100-mm height. It contained 20,863 nodes, corresponding to 107,918 linear tetrahedral elements. For the reconstruction basis, another mesh was used that was of the same geometry but contained 1076 nodes, corresponding to 4151 linear tetrahedral elements. The reconstruction time after the initial calibration procedure was approximately 20 min/per iteration on a 1.7-GHz PC with 2 Gbytes of RAM.

The reconstructed images at the 10th iteration are shown in Fig. 5. In Fig. 5, both  $\mu_a$  and  $\mu_s'$  images have been reconstructed with minimum background artifact. The calculated background  $\mu_a$  is  $0.0042 \text{ mm}^{-1}$ , and  $\mu_s'$  is  $0.978 \text{ mm}^{-1}$ , which corresponds well to the Intralipid solution used in the phantom. However, because an anomaly of unknown  $\mu_a$  and  $\mu_s'$  was used, a correct quantification cannot be estimated adequately. Furthermore, the peak  $\mu_a$  value corresponds to a position of  $x = 21.34 \text{ mm}$ ,  $y = 0.64 \text{ mm}$ ,  $z = -2.42 \text{ mm}$ , compared to the actual phantom position of  $x = 21 \text{ mm}$ ,  $y = 0 \text{ mm}$ ,  $z = 0 \text{ mm}$ .

#### C. Reconstruction from Clinical Patient Data

We describe the clinical and NIR imaging of a 73-year-old female subject. The patient presented for standard screening mammography, which revealed a subtle 25-mm asymmetric nodular density and associated architectural distortion in the lateral aspect of the left breast [see Fig. 6(a)]. Sonography of that site verified a hypoechoic solid mass with acoustic attenuation [Fig. 6(b)], which was clinically palpable. A subsequent 11-gauge core needle biopsy obtained with sonographic guidance demonstrated invasive breast carcinoma. A 2-mm stainless-steel site

marker [Micromark 2 tm (Ethicon)] was placed at the time of the needle biopsy. NIR imaging occurred 2 weeks after the biopsy procedure. One week later the patient underwent wide local (surgical) excision and sentinel lymphadenectomy of the left axilla. Pathology showed a 59-mm invasive carcinoma without (0/2) sentinel nodal involvement.

For the NIR exam the attendant brought the fiber-optic imaging array into direct contact with the breast at the level of the clinical abnormality. We obtained three tomographic acquisitions centered at the tumor site, with contiguous slices above (13 mm) and below (9 mm) the primary plane of interest, as indicated in Fig. 7. A single tomographic acquisition was performed of the contralateral breast in the mirror image (of the tumor) coronal location. Measurements collected from a cylindrical phantom at each wavelength were also recorded for calibration purposes.

From knowledge of the diameter of each measurement plane and of the separation between planes, we constructed a conical shaped mesh [see Fig. 8(a)]. The mesh contained 7898 nodes, corresponding to 38,725 linear tetrahedral elements. For image reconstruction, each data set (three planes at four wavelengths) was calibrated for each wavelength according to the procedures described above. The homogeneous (global) optical parameters that were calculated at each wavelength and used as an initial guess for the reconstruction are listed in Table 1. For the reconstruction basis a second mesh of the same geometry was used, which contained 3667 nodes, corresponding to 16,556 linear tetrahedral elements [Fig. 8(b)]. The reconstruction time after the initial calibration procedure was approximately 10 min/iteration on a 1.7-GHz PC with 2 Gbits of RAM.

Figures 9 and 10 show cross sections of 3D reconstructed images of  $\mu_a$  and  $\mu_s'$ , respectively, at each

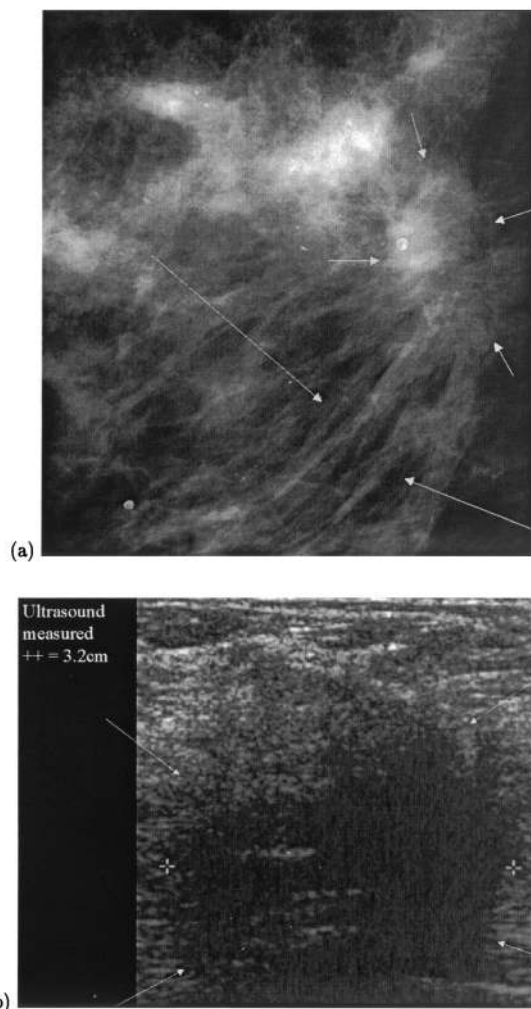


Fig. 6. Conventional breast imaging of a left breast carcinoma. (a) Photographically magnified left mediolateral mammogram. Short arrows, poorly defined central tumor mass; long arrows, associated architectural distortion consisting of long lines radiating from the tumor. (b) Sonography in the longitudinal plane reveals a hypoechoic mass (arrows), and calipers (+) measure the maximal diameter of the tumor at 3.2 cm.

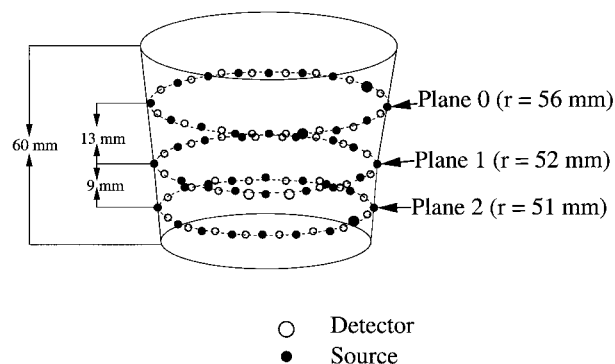


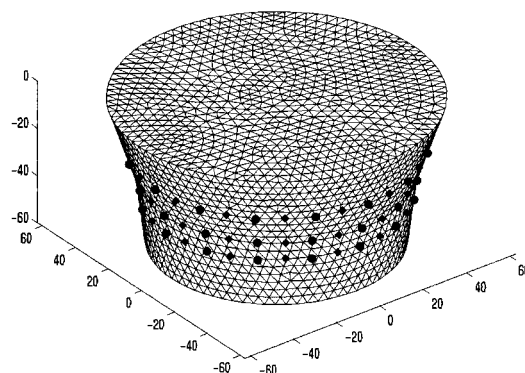
Fig. 7. Diagram of the setup used for the data collection from the volunteer. Measurements were made one plane at a time, with the midplane positioned at the midline of the lesion. In each case the radius of the measurement plane was recorded, as well as the separation between each plane. For mesh generation, 20 mm was allowed below and above the top and bottom planes of the fiber optic array.

Table 1. Computed Global Values of Absorption and Scattering Coefficients for Breast Data<sup>a</sup>

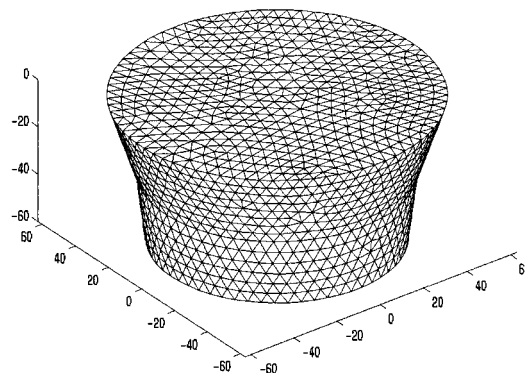
Wavelength (nm)	Global $\mu_a$ (mm <sup>-1</sup> )	Global $\mu_s'$ (mm <sup>-1</sup> )
761	0.0044	0.9355
785	0.0033	0.9519
808	0.0033	0.9365
826	0.0039	0.9153

<sup>a</sup>The values were calculated at each wavelength from the averaged data measured in each plane.

wavelength at the 10th iteration. Each of these cross sections is a coronal slice, starting from the nipple (leftmost image) and moving toward the chest wall (rightmost image), with the primary plane of interest being the third image from the left. It can be seen from the reconstructed  $\mu_a$  images in Fig. 9 that the anomaly appears with remarkable clarity. Furthermore, background noise appears to be minimal, with the images from 761 nm showing the great-



(a)



(b)

Fig. 8. Mesh used for the reconstruction of images from measured clinical data. The information shown in Fig. 7 was used for mesh generation. (a) Conical shaped mesh used for the calculation of the Jacobian, which contains 7898 nodes, corresponding to 38,725 linear tetrahedral elements. (b) Conical shaped mesh used for the reconstruction basis, which contains 3667 nodes, corresponding to 16,556 linear tetrahedral elements.

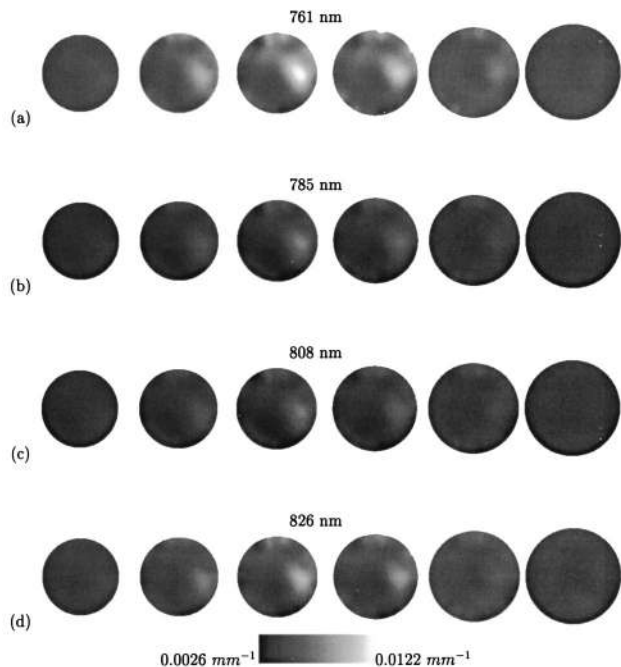


Fig. 9. Reconstructed images of  $\mu_a$  at each wavelength from measured volunteer data; each slice represents a plane through the mesh, from the bottom near the nipple (leftmost image) to the top near the chest (rightmost image). The images are coronal views of the cross section through the breast at the tenth iteration at the wavelengths indicated.

est absorption, at  $\mu_a = 0.0122 \text{ mm}^{-1}$ , at the plane of interest.

In Fig. 11, property profile transects of  $\mu_a$  and  $\mu_s'$  are shown through the primary plane of interest (third image from left, Figs. 9 and 10) at  $y = 0 \text{ mm}$ .

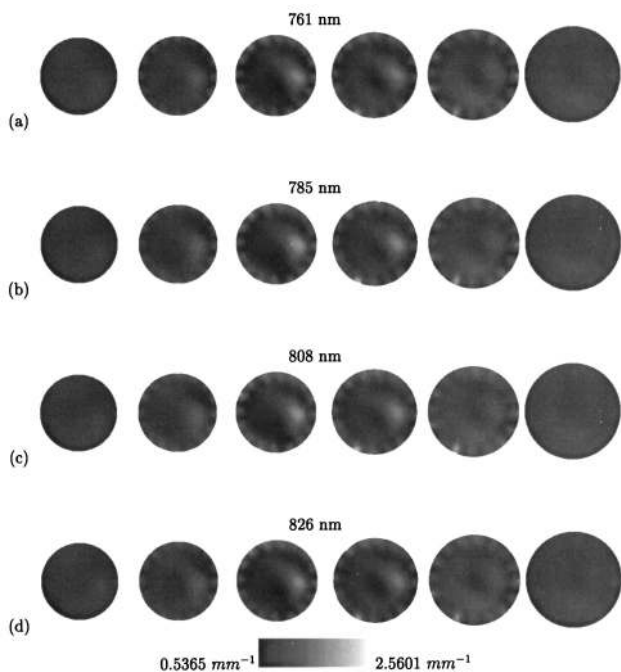


Fig. 10. Same as Fig. 9 but for  $\mu_s'$ .

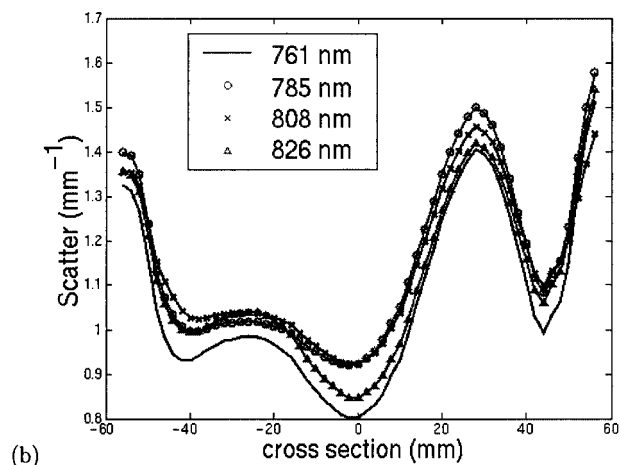
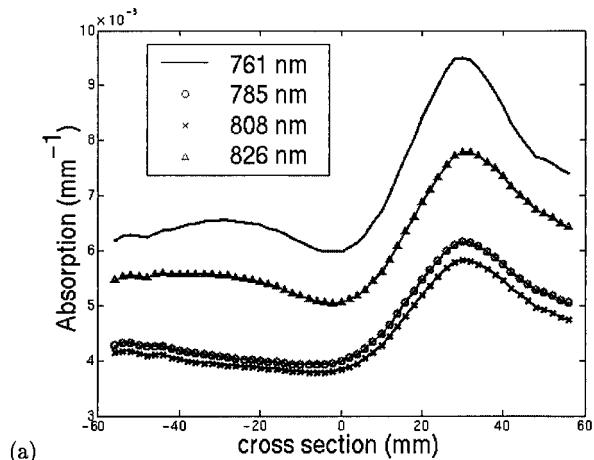


Fig. 11. Property profile transects through the  $\mu_a$  and  $\mu_s'$  images shown in Figs. 9 and 10. In each case the third slice from the left, extending through the plane of interest at  $y = 0 \text{ mm}$ , has been used. The position of the anomaly in these plots is at  $x = 27.5 \text{ mm}$ .

These plots show that  $\mu_a$  in the region of interest is dependent on the wavelength of the input light as well as on anomaly resolution and contrast. The image from 761 nm exhibits the greatest response, whereas the 808-nm data reveal the minimum response. This result is not surprising because the amount of absorption of the various chromophores varies with wavelength. In Fig. 11(b) the corresponding  $\mu_s'$  profile transects are shown. It is interesting to note that the scattering properties of the region of interest also seem to vary as a function of wavelength but not with so much dependence as the  $\mu_a$  properties. From the cross section for the  $\mu_a$  image at 761 nm shown in Fig. 11(a), we can estimate a full width at half-maximum value for the region of interest (measured as the maximum value against an overall average value for the background) of approximately 30 mm. This value, compared with the tumor's actual diameter of 32 mm as measured sonographically, is remarkable.

Finally, as we have multiwavelength data and, as



**Table 2.** Extinction Coefficients Used to Calculate Hb and HbO<sub>2</sub> Concentrations from Absorption Values at Each Wavelength for Breast Data

Wavelength (nm)	Hb [(mM) <sup>-1</sup> mm <sup>-1</sup> ]	HbO <sub>2</sub> [(mM) <sup>-1</sup> mm <sup>-1</sup> ]
761	0.3500	0.1515
785	0.2300	0.1800
808	0.1850	0.2080
826	0.1795	0.2275

shown, have reconstructed multiwavelength  $\mu_a$  images, it is possible to use these, together with published extinction coefficients for Hb and HbO<sub>2</sub> (Ref. 29; see Table 2) to calculate Hb and HbO<sub>2</sub> distributions because

$$\mu_{a(\lambda_i)} = \sum_{n=1}^N \epsilon_n(\lambda_i) c_n, \quad (8)$$

where  $i$  is the wavelength number ( $\lambda$ ),  $N$  is the number of chromophores,  $\epsilon$  is the extinction coefficient, and  $c$  is the chromophore concentration. Figures 12(a) and 12(b) show the calculated Hb and HbO<sub>2</sub> maps, respectively. These were calculated from

$$[\text{Hb}(j)\text{HbO}_2(j)] = \frac{\mu_{a(j,\lambda_i)}}{[\epsilon_{\text{Hb}(\lambda_i)}\epsilon_{\text{HbO}_2(\lambda_i)}]}, \quad (9)$$

where  $j$  is the reconstructed node throughout the whole volume.

The region of interest, the tumor position, shows a large Hb concentration of 22.9  $\mu\text{M}$ , compared with an average of 11.06  $\mu\text{M}$  within the background. Also, the calculated HbO<sub>2</sub> concentration has a peak value of 21.7  $\mu\text{M}$  in the region of the tumor, compared with 11.37  $\mu\text{M}$  for the background average. The calculated values of Hb and HbO<sub>2</sub> can be used to create the

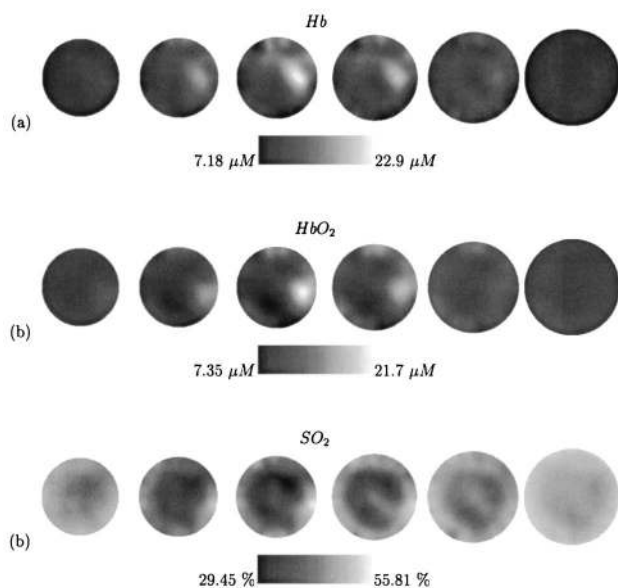


**Fig. 12.** Reconstructed images of Hb, HbO<sub>2</sub>, and SO<sub>2</sub> from the calculated  $\mu_a$  images shown in Fig. 9.

SO<sub>2</sub> distribution map, where  $\text{SO}_2 = \text{HbO}_2/(\text{HbO}_2 + \text{Hb})$  [Fig. 12(c)]. In this image the position of the tumor is shown as having a higher SO<sub>2</sub> level than the background.

#### 4. Discussion

We have presented our current method for 3D modeling of NIR light transport in tissue, together with algorithms for image reconstruction from both simulated and measured boundary data.

We have described a simulation study in which a 3D cylindrical phantom was modeled together with two anomalies (a single  $\mu_a$  and a single  $\mu_s'$  anomaly) situated deep inside. 3D data were calculated for 3 planes of measurements with 16 sources and detectors in each plane. We limited measurements to in-plane recordings only, to mimic our present instrumentation capabilities more closely, which produced 240 phase and amplitude measurements from each plane, giving rise to a total of 720 pieces of information. From these measurements, images were reconstructed with a Levenberg–Marquardt algorithm. From the reconstructed images (at iteration number 9) it is apparent that the reconstruction algorithm successfully recovers both anomalies with good localization and property separation (Fig. 2). The quantitative values recovered are not so good at this point; however, similar findings were reported previously.<sup>4</sup> If the algorithm is modified to include out-of-plane data, together with more-sophisticated regularization and addition of *a priori* information regarding the domain, the quantification of the reconstruction may improve.

Reconstructed images from a phantom study were presented in which a single shiny black marble was suspended in a hollow cylindrical phantom filled with an Intralipid solution of known  $\mu_a$  and  $\mu_s'$ . The localization of the inclusion was found to be only 1–2 mm from its true position, but, because an object of unknown optical properties was used, no conclusions about quantification can be made at this time. However, the calculated background  $\mu_a$  and  $\mu_s'$  for the Intralipid phantom showed good agreement with the expected values.

Reconstructed images from a clinical breast exam have been presented. Multiwavelength 3D NIR data were collected from a 73-year-old female volunteer who presented a 25-mm asymmetric density at mammography. Simultaneously reconstructed images of  $\mu_a$  and  $\mu_s'$  revealed absorbing and scattering anomalies at a location that corresponded to the expected region of disease (Figs. 9 and 10, respectively). The reconstructed  $\mu_a$  images showed dependence on the wavelength of the light used. The  $\mu_a$  images at 761 nm produced the greatest response. The reconstructed  $\mu_s'$  images also showed a dependence on wavelength but on a smaller scale relative to the  $\mu_a$  images (Fig. 11). There are also small boundary artifacts within the  $\mu_s'$  images at the detector position, but their magnitude is much smaller than the reconstructed anomaly. These artifacts can be reduced by

the use of additional filtering and incorporation of appropriate smoothing functions.

Because multiwavelength data were collected, it was possible to calculate concentrations of two chromophores, Hb and HbO<sub>2</sub> (Fig. 12) from the calculated  $\mu_a$  and the published extinction coefficients of these chromophores (Table 2). From these maps it is clear that the region of interest, the tumor position, presented a large Hb concentration compared with the background. The calculated HbO<sub>2</sub> concentration also revealed a peak at the location of the tumor. From the calculated Hb and HbO<sub>2</sub> maps, the oxygen saturation distribution was computed, which produced a higher SO<sub>2</sub> value in the region of the tumor relative to the background. Additionally, in the SO<sub>2</sub> image there is a high saturation anomaly at the boundary near the tumor, which may be due to bruising caused by the biopsy exam performed a week earlier. It can be certain that this artifact is not due to detector anomalies because such an artifact was seen only within the  $\mu_s'$  images, whereas the  $\mu_a$  images were used for the calculation of Hb, HbO<sub>2</sub>, and SO<sub>2</sub> maps. However, the origin of the anomaly warrants further investigation.

These results of high Hb, HbO<sub>2</sub>, and SO<sub>2</sub> are significant, as it is expected that a malignant tumor will be high in both blood content and blood oxygen saturation level. It is important to note that, whereas the total Hb concentration in the anomaly may currently be limited by the ability to reconstruct the true  $\mu_a$  values, the SO<sub>2</sub> saturation value could be an accurate representation because SO<sub>2</sub> saturation is a measurement of the ratio of oxygenated and total blood levels. Further studies to investigate this effect more accurately are required.

## 5. Conclusion

Three-dimensional multiwavelength near-infrared tomography has the promise and potential to provide physiological information about tissues and is a low-cost and hazard-free imaging technique. We have introduced, discussed, and presented our first reconstructed 3D data. The results presented include a simulation study, a simple phantom experiment, and also reconstructed images of  $\mu_a$ ,  $\mu_s'$ , Hb, HbO<sub>2</sub>, and SO<sub>2</sub> from a clinical breast exam.

We have shown that our modeling and reconstruction algorithm can produce fast and reliable images of internal optical properties, with good separation of  $\mu_a$  and  $\mu_s'$  regions and good localization with relatively fast computation time. The quantitative values from the reconstructed images are not so good as we had hoped for; however, this outcome may be a result of 3D imaging without out-of-plane data and as such can be considered a work in progress. To our knowledge, we have presented here the first clinical 3D reconstruction of  $\mu_a$ ,  $\mu_s'$ , Hb, HbO<sub>2</sub>, and SO<sub>2</sub> from multiwavelength NIR tomographic data collected from a human volunteer by use of a frequency modulated system. The results show promise, and we aim to be able to collect, reconstruct, and present multiple sets of clinical patient data in the future.

This research has been sponsored by the National Cancer Institute through grants RO1CA69544 and PO1CA80139.

## References

1. B. W. Pogue, K. D. Paulsen, C. Abele, and H. Kaufman, "Calibration of near-infrared frequency-domain tissue spectroscopy for absolute absorption coefficient quantitation in neonatal head-simulating phantoms," *J. Biomed. Opt.* **5**, 185–193 (2000).
2. B. W. Pogue, S. Geimer, T. McBride, S. Jiang, U. L. Osterberg, and K. D. Paulsen, "3-D simulation of near-infrared diffusion in tissue: boundary conditions and geometry analysis for a finite element reconstruction algorithm," *Appl. Opt.* **40**, 588–600 (2001).
3. T. O. McBride, B. W. Pogue, S. Jiang, U. L. Osterberg, K. D. Paulsen, and S. P. Poplack, "Multi-spectral near-infrared tomography: a case study in compensating for water and lipid content in hemoglobin imaging of the breast," *J. Biomed. Opt.* **7**, 72–79 (2002).
4. J. C. Hebden, H. Veenstra, H. Dehghani, E. M. C. Hillman, M. Schweiger, S. R. Arridge, and D. T. Delpy, "Three dimensional time-resolved optical tomography of a conical breast phantom," *Appl. Opt.* **40**, 3278–3287 (2001).
5. E. M. C. Hillman, J. C. Hebden, M. Schweiger, H. Dehghani, F. E. W. Schmidt, D. T. Delpy, and S. R. Arridge, "Time resolved optical tomography of the human forearm," *Phys. Med. Biol.* **46**, 1117–1130 (2001).
6. S. Fantini, M. A. Franceschini, E. Gratton, D. Hueber, W. Rosenfeld, D. Maulik, P. G. Stubblefield, and M. R. Stankovic, "Non-invasive optical mapping of the piglet in real time," *Opt. Express* **4**, 308–314 (1999), <http://www.opticsexpress.org>.
7. H. Eda, I. Oda, Y. Ito, Y. Wada, Y. Oikawa, Y. Tsunazawa, Y. Tsuchiya, Y. Yamashita, M. Oda, A. Sassaroli, Y. Yamada, and M. Tamaru, "Multichannel time-resolved optical tomographic imaging system," *Rev. Sci. Instrum.* **70**, 3595–3602 (1999).
8. D. A. Boas, D. H. Brooks, E. L. Miller, C. A. DiMarzio, M. Kilmer, R. J. Gaudette, and Q. Zhang, "Imaging the body with diffuse optical tomography," *IEEE Signal Proc. Mag.* **18**, 57–75 (2001).
9. J. C. Schotland and V. A. Markel, "Inverse scattering with diffusing waves," *J. Opt. Soc. Am. A* **18**, 2767–2777 (2001).
10. V. Ntziachristos, A. H. Hielscher, A. G. Yodh, and B. Chance, "Diffuse optical tomography of highly heterogeneous media," *IEEE Trans. Med. Imaging* **20**, 470–478 (2001).
11. H. Jiang, Y. Xu, N. Iftimia, J. Eggert, K. Klove, L. Baron, and L. Fajardo, "Three-dimensional optical tomographic imaging of breast in a human subject," *IEEE Trans. Med. Imaging* **20**, 1334–1340 (2001).
12. T. O. McBride, B. W. Pogue, S. Jiang, U. L. Osterberg, and K. D. Paulsen, "A parallel-detection frequency-domain near-infrared tomography system for hemoglobin imaging of the breast *in vivo*," *Rev. Sci. Instrum.* **72**, 1817–1824 (2001).
13. S. R. Arridge, "Topical review: optical tomography in medical imaging," *Inverse Probl.* **15**, R41–R93 (1999).
14. H. B. Jiang, K. D. Paulsen, U. L. Osterberg, and M. S. Patterson, "Frequency-domain optical image reconstruction in turbid media: an experimental study of single-target detectability," *Appl. Opt.* **36**, 52–63 (1997).
15. T. O. McBride, B. W. Pogue, U. L. Osterberg, and K. D. Paulsen, "Image reconstruction of continuously varying objects and simulated breast cancer lesions," in *Optical Tomography and Spectroscopy of Tissue III*, B. Chance, R. Alfano, and B. Tromberg, eds., *Proc. SPIE* **3597**, 514–525 (1999).
16. B. W. Pogue, S. P. Poplack, T. O. McBride, W. A. Wells, K. S. Osterman, U. L. Osterberg, and K. D. Paulsen, "Quantitative hemoglobin tomography with diffuse near-infrared spectroscopy," *IEEE Trans. Med. Imaging* **20**, 1334–1340 (2001).

- copy: pilot results in the breast," *Radiology* **218**, 261–266 (2001).
17. C. H. Schmitz, H. L. Graber, H. Luo, I. Arif, J. Hira, Y. Pei, A. Bluestone, S. Zhong, R. Andronica, I. Soller, N. Ramirez, S. S. Barbour, and R. L. Barbour, "Instrumentation and calibration protocol for imaging dynamic features in dense-scattering media by optical tomography," *Appl. Opt.* **39**, 6466–6486 (2000).
18. V. Ntziachristos, A. G. Yodh, M. Schnall, and B. Chance, "Concurrent MRI and diffuse optical tomography of breast after indocyanine green enhancement," *Proc. Natl. Acad. Sci. USA* **97**, 2767–2772 (2000).
19. Y. Painchaud, A. Mailloux, M. Morin, S. Verrault, and P. Beaudry, "Time domain optical imaging: discrimination between absorption and scattering," *Appl. Opt.* **38**, 3686–3693 (1999).
20. S. B. Colak, M. B. van der Mark, G. W. t'Hooft, J. H. Hoogenraad, H. S. van der Linden, and F. A. Kuijpers, "Clinical optical tomography and NIR spectroscopy for breast cancer detection," *IEEE J. Sel. Top. Quantum Electron.* **5**, 1143–1158 (1999).
21. M. Schweiger, S. R. Arridge, M. Hiraoka, and D. T. Delpy, "The finite element model for the propagation of light in scattering media: boundary and source conditions," *Med. Phys.* **22**, 1779–1792 (1995).
22. H. Jiang, K. D. Paulsen, U. L. Osterberg, B. W. Pogue, and M. S. Patterson, "Optical image reconstruction using frequency-domain data: simulations and experiments," *J. Opt. Soc. Am. A* **13**, 253–266 (1996).
23. S. R. Arridge, M. Schweiger, M. Hiraoka, and D. T. Delpy, "A finite element approach for modeling photon transport in tissue," *Med. Phys.* **20**, 299–309 (1993).
24. K. D. Paulsen and H. Jiang, "Spatially varying optical property reconstruction using a finite element diffusion equation approximation," *Med. Phys.* **22**, 691–701 (1995).
25. S. R. Arridge and M. Schweiger, "Photon-measurement density functions. 2. Finite-element-method calculations," *Appl. Opt.* **34**, 8026–8037 (1995).
26. P. P. B. Eggermort, G. T. Herman, and A. Lent, "Iterative algorithms for large partitioned systems, with application to image reconstruction," *Linear Algebra Appl.* **40**, 37–67 (1981).
27. T. O. McBride, "Spectroscopic reconstructed near infrared tomographic imaging for breast cancer diagnosis," Ph.D. dissertation (Dartmouth College, Hanover, N.H. 2001).
28. J. Schoberl, "NETGEN—an automatic 3D tetrahedral mesh generator," <http://www.sfb013.uni-linz.ac.at/joachim/netgen/>.
29. S. Wray, M. Cope, D. T. Delpy, J. S. Wyatt, and E. Reynolds, "Characterization of the near infrared absorption spectra of cytochrome *aa3* and hemoglobin for the noninvasive monitoring of cerebral oxygenation," *Biochim. Biophys. Acta* **933**, 184–192 (1988).